Computational modeling of photoacoustic signals from mixtures of melanoma and red blood cells

Ratan K. Saha[a)]
Surface Physics and Material Science Division, Saha Institute of Nuclear Physics, 1/AF Bidhannagar, Kolkata 700064, India

(Received 24 February 2014; revised 20 June 2014; accepted 16 August 2014)

A theoretical approach to model photoacoustic (PA) signals from mixtures of melanoma cells (MCs) and red blood cells (RBCs) is discussed. The PA signal from a cell approximated as a fluid sphere was evaluated using a frequency domain method. The tiny signals from individual cells were summed up obtaining the resultant PA signal. The local signal to noise ratio for a MC was about 5.32 and 5.40 for 639 and 822 nm illuminations, respectively. The PA amplitude exhibited a monotonic rise with increasing number of MCs for each incident radiation. The power spectral lines also demonstrated similar variations over a large frequency range (5–200 MHz). For instance, spectral intensity was observed to be 5.5 and 4.0 dB greater at 7.5 MHz for a diseased sample containing 1 MC and 22 952 RBCs than a normal sample composed of 22 958 RBCs at those irradiations, respectively. The envelope histograms generated from PA signals for mixtures of small numbers of MCs and large numbers of RBCs seemed to obey pre-Rayleigh statistics. The generalized gamma distribution found to facilitate better fits to the histograms than the Rayleigh and Nakagami distributions. The model provides a means to study PAs from mixtures of different populations of absorbers. © *2014 Acoustical Society of America*. [http://dx.doi.org/10.1121/1.4894794]

PACS number(s): 43.80.Qf, 43.35.Ud, 43.80.Cs [MDV] Pages: 2039–2049

I. INTRODUCTION

Metastasis is a complex process that involves spread of a tumor or cancer from its original site to distant parts of the body.[1,2] The cancer cells are prone to metastasize because they generally grow very rapidly in an unregulated manner and lose their ability to adhere to one another.[3] As a result of that, the cells can easily move from one place to another place through our lymphatic or blood circulatory systems. The tumor cells that are flowing with the blood stream are known as circulating tumor cells (CTCs). The detection, isolation, and characterization of CTCs are of enormous importance to diagnose and stage the disease and eventually to direct preventive treatments. CTCs exist within the blood stream in an extraordinarily low number (approximately one CTC in one ml of blood).[4] That makes it extremely difficult to isolate a CTC from billions of red blood cells (RBCs) with the available technologies. Consequently, these cells have not been characterized fully yet.[1]

Several methods have been developed to detect CTCs in the blood stream.[1] For example, nucleic acid-based techniques have been explored; CTCs have also been distinguished from normal blood corpuscles based on their physical properties. In addition to that, efforts have been made to detect CTCs by exploiting photoacoustic (PA) effect (i.e., the generation of sound due to absorption of light).[5–8] In the last 10 years, PA technique has developed a lot and found important applications in biomedical imaging. By detecting optically induced ultrasonic waves, better resolution and depths of more than ∼1 mm are easily achieved due to weaker scattering of sound waves than that of light in tissue (scattering of acoustic waves in tissue is 2 to 3 orders of magnitude less than that of light).[9] Wang *et al.* capitalized functional imaging capacity of this technique with a great success.[5–8] For instance, cerebral hemodynamics of rat brain in response to one-sided whisker stimulation was mapped using PA tomography.[5] Additionally, exquisite images of vasculature of human palm and skin were produced by this group.[6] They also performed *in vivo* imaging of a subcutaneously inoculated B16-melanoma in an immunocompromised nude mouse at 584 and 764 nm. A combined image revealed the 3D morphology of both the melanoma and the surrounding vasculature.[6] Melanoma cells (MCs) are generally rich in melanin and that causes a MC to be a much stronger PA source than a RBC at certain bands of incident laser radiation. For example, optical absorption coefficient for melanin contained within melanosome in human skin specimens is about 125 cm^{-1} at 800 nm,[10,11] but the same quantity at that wavelength for hemoglobin (Hb) is approximately 4 cm^{-1} at a concentration of 150 g Hb/liter.[11] This fact essentially leads to the believe that it would be possible to detect MCs in blood stream with PAs.

Viator and his colleagues detected the PA signals from human malignant MC line HTB-67 SK-MEL-l suspended in a saline solution using a circulatory system designed and developed by them.[3,12] The solution was circulated at a rate of 0.15 ml/s and was illuminated with a 450 nm laser beam. On the basis of experimental results, they concluded that the PA detection mechanism has the ability to detect small numbers of malanotic MCs in the test solution *in vitro*. Zharov group[13] has recently reported the development of a time resolved PA flow cytometry setup. They performed rigorous experiments with HTB-65 and MALME-3M human MCs

a)Author to whom correspondence should be addressed. Electronic mail: ratank.saha@saha.ac.in

and B16F10 mouse MCs under *in vitro* and *in vivo* conditions. According to their data, PA system is capable of detecting single CTC in the presence of approximately 1000 RBCs in the irradiated volume at 850 nm. Solano *et al.*[14] measured the PA signals from a series of monolayers of different cell lines *in vitro*. They observed that the MC line HS936 produced a detectable PA signal in which the PA amplitude was dependent on the number of cells. They also computed the PA signals from monolayers using a time domain approach. The simulated PA amplitude was found to be correlated with the number of cells in the monolayer as noticed in the experiment.

Recently a theoretical framework has been developed to express the PA signal generated by a collection of cells.[15] In this model, cells were treated as fluid spheres packaging chromophores and a frequency domain approach was used to evaluate the PA signal from each sphere. The underlying assumption is that the optical absorption takes place at the molecular level but acoustic emission takes place at the cellular level. The tiny signals emitted by the individual spheres were linearly superimposed to obtain the resultant PA signal. This model has been successfully explored in the framework of forward problem formulation. For example, it was utilized to examine the effect of RBC aggregation on the PA signals. It predicted that the PA amplitude would increase with increasing aggregation.[15] The validity of the prediction was confirmed by conducting *in vitro* experiments with human and porcine RBCs.[16,17] The framework was also used to investigate the PAs of mixtures of oxygenated and deoxygenated RBCs and provided results consistent with that of experiments.[18] The possibility of using the PA technique to differentiate intraerythrocytic stages of malarial parasite was examined using this theoretical tool.[19] It was shown that it would be possible to stage intraerythrocytic development of malarial parasite with the PA technique if appropriate optical illuminations are used to excite the cells. PAs of cancer cells with endocytosed gold nanoparticles was studied as well.[20] It was illustrated that the PA signal amplitude increased monotonically with cell concentration, which is in accordance with experimental findings.[21]

It may be emphasized that the theoretical framework models tissue as a collection of discrete absorbers and reveals that ultrasonic spectral domain features of PA signals depend on the properties of tissue microstructures. For example, spatial organization, size distribution, concentration, biophysical, and biochemical states of the absorbers are the intrinsic factors that control spectral power distribution of PA signals. Recent experimental studies also reported that these parameters can influence PA spectral characteristics.[17,22–24] These theoretical and experimental findings essentially opened up a possibility that tissue characterization might be feasible with PAs. Wang *et al.* accurately assessed the dimensions of microparticles hidden in turbid phantoms using a spatial auto-correlation function to perform PA spectral analysis.[25] This study also concluded that PA spectral analysis could be a potential tool for characterizing microstructures in biological samples. Note that ultrasonic tissue characterization is an established technique.[26,27] Various correlation functions, such as fluid sphere, spherical shell, and the Gaussian models, have been used in that context to analyze radio frequency echo signal power spectrum to quantify average physical properties of tissue microstructures.

The focus of the paper is to explore the theoretical model in the forward problem formulation to examine PAs of samples composed of different populations of absorbers with size dispersity and different physical properties. Essentially, the PA signals from mixtures of MCs and RBCs were investigated. The framework has never been used to study PAs of a polydisperse system. Previous studies dealt with monodisperse absorbers.[15,18,19] The spatially random distributions of cells in 3D were generated by employing a Monte Carlo method. The simulated signals were analyzed to extract time and frequency domain properties as a function of number of MCs present within the irradiated blood volume. The statistics of the PA signals from different mixtures of MCs and RBCs were also investigated. The capability of the Rayleigh, Nakagami, and generalized gamma distribution functions to model envelope histograms were examined and to the best of our knowledge, that has never been reported in literature. It was shown that the theoretical model provided physically meaningful results. Further, sufficient insights about the PAs of mixtures of light absorbing cells can be gained from this study.

The organization of the paper is as follows. Section II discusses the theoretical framework. The computational steps are described in Sec. III. Various probability distribution functions (pdfs) are also elaborated in this section. In Sec. IV, the computational results are presented. The modeling approach and the results of this work are elucidated in Sec. V in the light of reported theoretical and experimental results. The conclusions of this study are also drawn in Sec. V.

II. THEORETICAL FOUNDATION

The theoretical formulation was reported in detail in some recent publications.[15–19] However, for the sake of completeness, the fundamentals are given below. The time dependent wave equation for the PA field can be derived using the linearized equations of fluid dynamics.[28] The condition of thermal confinement is imposed during the derivation of such a wave equation. It implies that the acoustic pulse is launched before significant thermal conduction takes place. The wave equation can be solved using Green's function method for both regular as well as irregular shapes of absorbing regions.[29]

On the other hand, the wave equation can be solved in frequency domain for a spherical absorber and the exact solution can be obtained by employing the boundary conditions (i.e., continuity of the pressure field and the normal component of the particle velocity at the spherical boundary). The expression for the PA field generated by a uniformly illuminated absorbing fluid sphere mimicking a cell surrounded by a nonabsorbing fluid medium can be cast as[28]

$$\tilde{p}^{\text{single}}(\mathbf{r},\,\omega) = \frac{i\mu_a \beta I_0 v_s a^2}{C_P}\,\phi\,\frac{e^{ik_f r}}{r}, \tag{1}$$

where

$$\phi = \frac{j_1(k_s a)e^{-ik_f a}}{\left[(1-\hat{\rho}_s)\dfrac{\sin(k_s a)}{k_s a} - \cos(k_s a) + i\hat{\rho}_s\hat{v}_s \sin(k_s a)\right]},$$
$$\hat{\rho}_s = \rho_s/\rho_f,\ \ \hat{v}_s = v_s/v_f,\ \ k_f = \omega/v_f,\ \ k_s = \omega/v_s. \tag{2}$$

Here, j_1 is the spherical Bessel function of first kind of order unity, ω is the modulation frequency of the optical beam with intensity I_0, and a is the radius of the spherical absorber. The notations μ_a, β, and C_P represent the light absorption coefficient, thermal expansion coefficient, and isobaric heat capacity per unit mass for the absorbing medium, respectively. Further, ρ_s and v_s refer to as the density and speed of sound for the absorbing medium, respectively. The same quantities for the surrounding medium are denoted by ρ_f and v_f, respectively. The wave numbers for the absorbing and the fluid medium are indicated by k_s and k_f, respectively. The superscript single is used to state that only one PA source is considered.

Consider an ensemble of absorbing fluid spheres suspended in a nonabsorbing fluid medium. The PA field generated by the suspension due to uniform illumination of the absorbers can be expressed as a linear superposition of tiny fields produced by the individual absorbers.[15–19] This is known as the single particle approach. This approach works well for sparse medium and has been successfully utilized in optical and ultrasonic scattering problems to interpret experimental results.[30,31] It has also been explored recently to explain PA experimental results qualitatively.[16,17] If the suspension contains a binary mixture of absorbing fluid spheres mimicking RBCs and MCs, the PA field in the far field in this framework can be cast as,[18]

$$\tilde{p}^{\text{many}}(\mathbf{r},\omega) \approx \left[\frac{i\mu_{ae}\beta_e I_0 v_e a_e^2}{C_{Pe}}\,\phi_e \sum_{l=1}^{N_e} e^{-i\mathbf{k}_f\cdot\mathbf{r}_{el}} + \frac{i\mu_{am}\beta_m I_0 v_m a_m^2}{C_{Pm}}\,\phi_m \sum_{n=1}^{N_m} e^{-i\mathbf{k}_f\cdot\mathbf{r}_{mn}}\right]\frac{e^{ik_f r}}{r}, \tag{3}$$

where

$$\phi_e = \frac{j_1(k_e a_e)e^{-ik_f a_e}}{\left[(1-\hat{\rho}_e)\dfrac{\sin(k_e a_e)}{k_e a_e} - \cos(k_e a_e) + i\hat{\rho}_e\hat{v}_e \sin(k_e a_e)\right]},$$
$$\hat{\rho}_e = \rho_e/\rho_f,\ \ \hat{v}_e = v_e/v_f,\ \ k_e = \omega/v_e, \tag{4}$$

and

$$\phi_m = \frac{j_1(k_m a_m)e^{-ik_f a_m}}{\left[(1-\hat{\rho}_m)\dfrac{\sin(k_m a_m)}{k_m a_m} - \cos(k_m a_m) + i\hat{\rho}_m\hat{v}_m \sin(k_m a_m)\right]},$$
$$\hat{\rho}_m = \rho_m/\rho_f,\ \hat{v}_m = v_m/v_f,\ k_m = \omega/v_m. \tag{5}$$

The subscripts e and m in Eq. (3) denote erythrocyte and melanocyte, respectively. Further, μ_{ae}, β_e, C_{Pe}, ρ_e, v_e, and k_e are the light absorption coefficient, thermal expansion coefficient, isobaric heat capacity per unit mass, density, speed of sound, and wave number for erythrocytes, respectively. The same quantities for MCs are represented by using the subscript m. In Eq. (3), a_e denotes the radius of an equivalent sphere of a RBC and a_m refers to the same for a MC. Moreover, N_e and N_m are the numbers of RBCs and MCs, respectively, that are present within the illuminated region. The wave vector $\mathbf{k}_f$ defines the direction of observation, $\mathbf{r}_{el}$ is the position vector for the lth RBC, and $\mathbf{r}_{mn}$ is the position vector for the nth MC. The corresponding geometry is shown in Fig. 1. The superscript, many states that the PA field is generated by a collection of sources. It can be noted that the contributions from erythrocytes and melanocytes are added in Eq. (3) to obtain the resultant PA field. Furthermore, multiple scattering of light and sound waves were ignored in this derivation.

The time dependent PA field for a delta function heating pulse can be obtained by taking the Fourier transformation of Eq. (3) and that yields

$$p^{\text{many}}(\mathbf{r},t) \approx \frac{iF}{2\pi}\int_{-\infty}^{\infty} d\omega\left[\frac{\mu_{ae}\beta_e v_e a_e^2}{C_{Pe}}\,\phi_e \sum_{l=1}^{N_e} e^{-i\mathbf{k}_f\cdot\mathbf{r}_{el}} + \frac{\mu_{am}\beta_m v_m a_m^2}{C_{Pm}}\,\phi_m \sum_{n=1}^{N_m} e^{-i\mathbf{k}_f\cdot\mathbf{r}_{mn}}\right]\frac{e^{ik_f(r-v_f t)}}{r}, \tag{6}$$

where F is the fluence of the incident optical beam. Equation (6) represents an analytic signal for which imaginary part is the Hilbert transform of real part. Equation (6) was computed in this work for different mixtures of RBCs and MCs to examine how the presence of melanocytes in the blood stream alters the PA signal properties.

III. COMPUTATIONAL APPROACH

A. Simulation of tissue realizations in 3D

The shape of an erythrocyte is biconcave under normal physiological conditions. However, each RBC in this study was approximated as a fluid sphere. It may be a valid

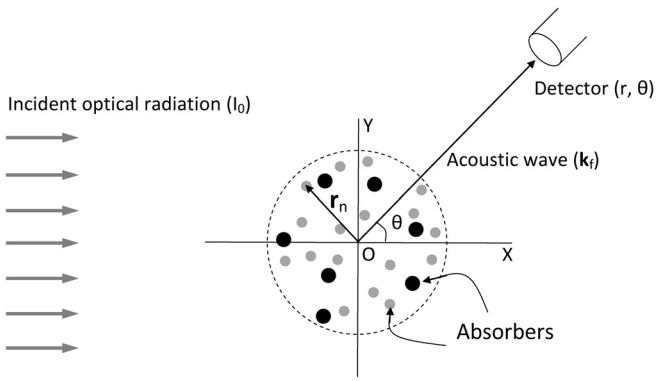

FIG. 1. A schematic diagram elaborating the PA geometry. The illuminated region is represented by the dashed circle. The small filled circles denote RBCs and big filled circles indicate MCs.

approximation in the diagnostic ultrasonic frequency range because in this range, wavelengths of the acoustic waves are much longer than the size of a RBC. The fluid spheres representing RBCs were suspended in saline water to simulate a blood sample. RBCs encapsulate hemoglobin molecules as chromophores and they are also much more numerous than other particles such as white blood cells and platelets (98% of blood particles are RBCs). Hence, they are the dominant light absorbing corpuscles in blood for the incident optical wavelengths that are generally used for PA experiments.[7] Moreover, the PA signals emitted by white blood cells and platelets were not considered in this study because their intrinsic light absorption is much smaller than RBCs and consequently, produce negligibly weak signals.[32,33] MCs also contribute to the PA signal when they are present within the illuminated volume [also referred to as the region of interest (ROI) in the text]. MCs were modeled as fluid spheres in some previous investigations.[13,14] This study, as well, treats MCs as fluid spheres. Melanocytes enclose melanin, which is, in general, a dark pigment and a strong absorber of light. The most common type of melanin is referred to as eumelanin, which is available in human skin and eyes. It appears as black to dark brown. It is an insoluble heterogeneous biopolymer.[34] On the other hand, another variety of melanin known as pheomelanin, looks yellow to reddish brown. It is an alkali-soluble material and can typically be found in mammalian hair and chicken feathers.[35] The third form of melanin is termed as neuromelanin, which is produced in specific populations of catecholaminergic neurons in the brain.[36]

Blood tissue was simulated by placing MCs and RBCs randomly within the ROI. The size of the ROI was fixed to $500 \times 100 \times 100$ μm^3. This volume was filled by cells to achieve a 40% packing fraction. This packing fraction was chosen because the fractional volume occupied by RBCs is close to 0.4 in human blood. A Monte Carlo algorithm known as the random sequential adsorption technique was employed to generate random locations of nonoverlapping particles.[37] The largest particles (i.e., MCs) were placed first within the ROI followed by the positioning of the smaller particles (i.e., RBCs). This is the procedure that is generally followed to generate configurations for spatially random distribution of spheres with size dispersity.[38,39] In order to generate the position coordinates of RBCs, entire ROI was divided into a number of sub-blocks of equal size ($500 \times 10 \times 10$ μm^3) and each sub-block was packed separately with RBCs. Each RBC attached to a sub-block did not overlap with other particles belonging to the same sub-block. RBCs locating at the boundaries of a sub-block additionally maintained nonoverlapping condition with RBCs belonging to the neighboring sub-blocks. RBCs also did not overlap with MCs. This simulation approach was adapted to construct a sufficiently big tissue volume within a realistic time frame. The procedure is described in detail in a recent publication.[19]

B. Quantitative values for various physical parameters

The volume of an equivalent sphere of a RBC was taken as 87 μm^3 with radius $a_e = 2.75$ μm. The density and speed of sound for a RBC were taken as $\rho_e = 1092$ kg/m^3 and $v_e = 1639$ m/s, respectively.[40] The thermal expansion coefficient and heat capacity per unit mass for an erythrocyte were assumed to be $\beta_e = 1.5 \times 10^{-4}$ K^{-1} and $C_{Pe} = 3.23 \times 10^3$ J kg^{-1}K^{-1}, respectively.[41] The optical absorption coefficient for the medium inside a RBC was estimated to be $\mu_{ae} = 1771.8$ and 1071.4 m^{-1} for 639 and 822 nm incident radiations, respectively. The PA signals generated at these two wavelengths were examined in this study. Note that similar wavelengths were employed in practice for *in vivo* detection of MCs with PAs.[13] The optical absorption coefficient for an erythrocyte was estimated by evaluating the relationship $\mu_{ae} = C_{\mathrm{HbO}_2}\epsilon_{\mathrm{HbO}_2} + C_{\mathrm{Hb}}\epsilon_{\mathrm{Hb}}$, where C_{HbO_2} and $\epsilon_{\mathrm{HbO}_2}$ are the molar concentration and the molar extinction coefficient for oxyhemoglobin molecules, respectively.[42] Analogous quantities for deoxyhemoglobin molecules are denoted by C_{Hb} and ϵ_{Hb}, respectively. The molar extinction coefficients for oxyhemoglobin and deoxyhemoglobin molecules could be found over a wide range of optical wavelengths in Ref. 11. On the other hand, an erythrocyte typically encloses 280×10^6 hemoglobin molecules and therefore, molar concentration can easily be computed to be 5.34 moles/l.[43] It was also assumed that blood oxygen saturation vis-à-vis RBC oxygen saturation remained to be 75% (i.e., similar to that of venous blood) for all samples investigated in this work. It might be noted that for such a level of oxygen saturation 75% of the hemoglobin molecules were oxygenated and 25% of them were deoxygenated.

The radius of a MC was taken as $a_m = 5.0$ μm.[14] The density and heat capacity per unit mass were assumed to be $\rho_m = 1150$ kg/ m^3 and $C_{Pm} = 2.81 \times 10^3$ J kg^{-1}K^{-1}, respectively.[10] The optical absorption coefficient was considered as $\mu_{am} = 29852.2$ and 11 979.4 m^{-1} for 639 and 822 nm optical illuminations, respectively.[10] The speed of sound and thermal expansion coefficient for MCs were not available in the literature and thus, were fixed similar to that of RBCs, i.e., $v_m = 1639$ m/s and $\beta_m = 1.5 \times 10^{-4}$ K^{-1}, respectively. The density and speed of sound for the ambient medium were set to $\rho_f = 1005$ kg/m^3 and $v_f = 1498$ m/s, respectively. Table I summarizes the numerical values considered for these parameters.

C. Generation of the PA signals

In this work, Eq. (6) was evaluated numerically to compute complex pressure for a mixture of RBCs and MCs at a distance 6000 μm from the center of the ROI and in the backward direction. The contributions from a wide range of frequencies (MHz to GHz) were summed up. The time series pressure data were generated at a sampling frequency of 4 GHz. The real parts of the time series data provided the radio frequency (RF) line. The signal amplitude at each time point was calculated from the square root of the sum of squares of the real and imaginary parts. The PA signals were simulated for various samples with increasing number of MCs. For each sample, 150 RF lines were computed from 150 different tissue configurations. The average power spectrum computed from 150 PA traces was obtained using central part of the signals for each sample to examine how the presence of MCs alters spectral features. The variation of

TABLE I. Quantitative values for various mechanical, thermal, and optical parameters.

ρ_f (kg/m^3)	1005
v_f (m/s)	1498
a_e, a_m (μm)	2.75, 5.0
ρ_e, ρ_m (kg/m^3)	1092, 1150
v_e, v_m (m/s)	1639, 1639
β_e, β_m (K^{-1})	1.5×10^{-4}, 1.5×10^{-4}
C_{Pe}, C_{Pm} (J kg^{-1}K^{-1})	3.23×10^3, 2.81×10^3
μ_{ae}, μ_{am} (m^{-1})	1771.8, 29 852.2 (at 639 nm)
μ_{ae}, μ_{am} (m^{-1})	1071.4, 11 979.4 (at 822 nm)
F (J m^{-2})	1

mean amplitude with MC concentration was also investigated in this work. A C code was developed for this purpose and executed in a personal computer [OS: Ubuntu 12.10; Processor: Intel(R) Core(TM) i3–2130 CPU, 3.40 GHz; RAM: 4 GB]. The execution time was about 8 h generating 150 lines. The simulated data were processed in MATLAB R2009b.

D. Statistics of the PA signals

The statistics of the PA signals generated by different mixtures of MCs and RBCs have also been studied in this work. The suitability of three different pdfs, namely, the Rayleigh, Nakagami, and generalized gamma to model the statistics of the envelope data have been examined.[44,45] The Rayleigh pdf is expressed as[44,46]

$$f(A) = \frac{A}{\sigma^2}\exp\left(-\frac{A^2}{2\sigma^2}\right), \quad A \geq 0, \ \ \sigma > 0, \tag{7}$$

where σ is the scale parameter. It is a single parameter pdf. In the context of ultrasonic tissue characterization, it has been successfully explored to describe envelope statistics of ultrasonic backscatter signals from an ensemble of large number of scatterers randomly located in space.

The Nakagami pdf is given by[44,46]

$$f(A) = \frac{2\xi^{\xi}A^{2\xi-1}}{\Gamma(\xi)\Omega^{\xi}}\exp\left(-\frac{\xi A^2}{\Omega}\right), \quad A \geq 0, \ \ \xi, \Omega > 0, \tag{8}$$

where Γ is the gamma function; Ω and ξ are the scale and shape parameters, respectively. It is a two-parameter pdf and applicable to model envelope statistics of many situations, ranging from pre-Rayleigh to Rayleigh to post-Rayleigh, encountered in medical ultrasonics. It has been found to be useful to classify tumors in the breast as benign or malignant.[46] The Rayleigh pdf is a special case of the Nakagami pdf ($\xi = 1$).

The generalized gamma pdf can be cast as[44,47]

$$f(A) = \frac{cA^{cu-1}}{\alpha^{cu}\Gamma(u)}\exp\left(-\frac{A^c}{\alpha^c}\right), \quad A \geq 0, \ \ \alpha, c, u \geq 0, \tag{9}$$

where α is the scale parameter; c and u are the shape parameters. It is a three-parameter function and has the ability to describe the statistics of ultrasonic backscatter signals from tissue in a much superior manner than any other distributions do.[44] Both the Rayleigh and Nakagami pdfs can be derived from the generalized gamma function. For example, Eq. (7) can be obtained by setting $c = 2$ and $u = 1$. Further, for $c = 2$, Eq. (9) reduces to Eq. (8). Raju *et al.*[44] studied the statistics of high frequency ultrasonic backscatter signals from *in vivo* normal human dermis and subcutaneous fat. The generalized gamma parameters showed significant differences between the dermis at the forearm and fingertip regions. Tunis *et al.*[47] investigated the use of signal envelope statistics to monitor and quantify structural changes during cell death and demonstrated that the generalized gamma fit parameters exhibited sensitivity to structural changes in the cells.

In this work, envelope histograms generated from wide bandwidth PA signals [computed from Eq. (6)] were fitted with these distribution functions. For each sample, central parts of 150 different PA lines simulated from 150 different configurations were used to calculate the average histogram. The best fit curves and thus the fitting parameters were obtained using a MATLAB optimization routine (fminsearch).

These pdfs were also utilized to model the envelope histograms constructed from band-limited (BL) signals. The envelope statistics of BL signals have been included in this work because PA signals are detected using a finite bandwidth transducer in practice. The BL signal can be calculated by convolving the wide bandwidth signal [Eq. (6)] with a Gaussian function mimicking the frequency response of a detector yielding[19]

$$p_{\mathrm{BL}}(\mathbf{r}, t) = \mathrm{Re}[p^{\mathrm{many}}(\mathbf{r}, t)] * h(t), \tag{10}$$

where $h(t) = (\tau/\sqrt{2\pi})e^{-(\tau^2t^2/2)}\cos(\omega_0 t)$ and $*$ represents the convolution operation. The center frequency and -6 dB bandwidth of the transducer are represented by ω_0 and τ, respectively. The BL signals were calculated for a 40 MHz transducer with 80% as the -6 dB bandwidth.

IV. COMPUTATIONAL RESULTS

Figure 2(a) shows a representative PA RF line (solid line) generated by a blood sample containing only one MC and 22952 RBCs, when illuminated by 639 nm optical beam. The associated signal envelope (dashed line) is also shown in the same figure. It can be observed that signal envelope fluctuates very rapidly and that is due to the presence of high frequency components. Very strong PA signals have been generated at each boundary due to coherent addition of tiny signals emitted by the individual cells situated adjacent to each boundary. Nevertheless, incoherent addition of acoustic waves produced by the randomly placed cells results in great reduction of signal amplitude at the central region. It can be noticed that there is a sudden increase in the signal amplitude at around 3950 ns. It has been originated from the MC. Two vertical lines have been used to highlight the signal produced by the MC and its neighboring RBCs. This portion is further elaborated in the inset for clarity. The signal to noise ratio (abbreviated as SNR and defined as peak amplitude/

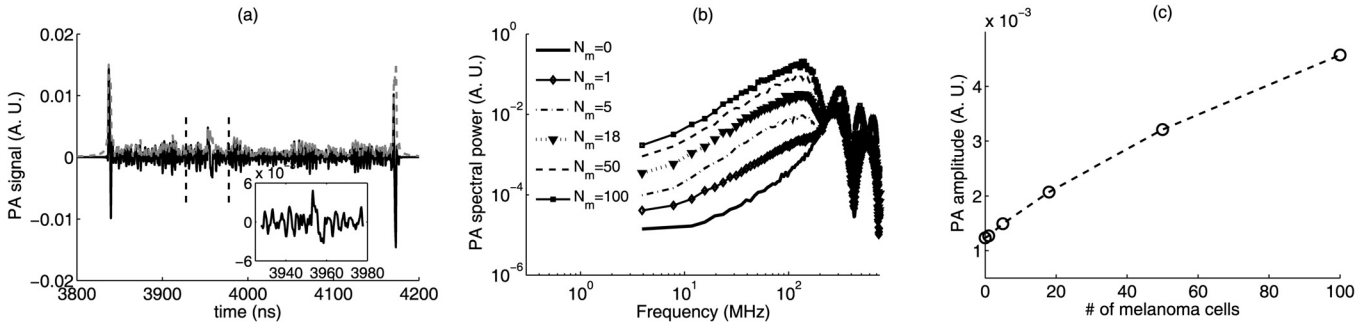

FIG. 2. (a) A representative PA RF line (solid line) and its envelope (dashed line) when 639 nm optical radiation is used to excite the sample containing only one MC and many RBCs. The gated region corresponds to the signal generated by the MC and its neighboring RBCs. It is further highlighted in the inset. The sudden increase in the PA amplitude is due to the MC. (b) The variations of power spectrum curves (averaged over 150 RF lines) over a wide range of frequencies (MHz to GHz) for various samples with increasing number of MCs. (c) The plot of the mean PA amplitude (evaluated from 150 RF lines) as a function of number of MCs present within a sample.

std[3]) for this region is approximately 5.32. The plots of power spectrum, averaged over 150 RF lines for each, are shown in Fig. 2(b) for a series of blood samples with increasing MCs. The solid line corresponding to $N_m = 0$ displays the power spectrum for a sample composed of RBCs only. The first minimum for this curve appears nearly at 426 MHz and that can be linked to the size of RBC. The spectral curve for $N_m = 1$ looks to be well separated from $N_m = 0$ line up to about 150 MHz. For example, the spectral intensity for $N_m = 1$ line is about 5.5 dB more than that of $N_m = 0$ line at 7.5 MHz. The contrast of MC with respect to RBCs is very high at this illumination, leading to two distinguishable lines up to 150 MHz. It is interesting to note that for curves with $N_m > 1$, the first minimum occurs approximately at 234 MHz. This minimum can be attributed to the size of MC. Additionally, as the number of MCs increases the spectral intensity also increases at each frequency up to the first maximum ($\approx$ at 150 MHz). For instance, it is about 23 dB higher for $N_m = 100$ line than $N_m = 0$ curve at each frequency up to 150 MHz. The variation of the PA amplitude is illustrated in Fig. 2(c) as a function of number of MCs present in a blood sample. It can be seen that the PA amplitude varies linearly with the number of MCs. Galanzha *et al.* also experimentally demonstrated linear variation of the PA amplitude with the number of MCs in the detected volume (Fig. 5(c) of Ref. 13).

A typical simulated trace of a PA RF line (solid line) is displayed in Fig. 3(a) when 822 nm laser source uniformly irradiates a mixture of MCs and RBCs ($N_m = 1$ and $N_e = 22952$). The amplitude variation is also demonstrated by the dashed line in the same figure. The RF line seems similar to that of Fig. 2(a). However, the PA amplitude is weaker in this case than that of 639 nm beam [see Fig. 2(a)]. This is because absorption of light by both types of cells (i.e., MCs and RBCs) is less at this wavelength in comparison to the other wavelength. The signal associated with the MC is marked by the two vertical lines and is also expanded in the inset. The signal to noise ratio is about 5.40 in this case. Figure 3(b) illustrates power spectrum curves for different mixtures of MCs and RBCs. In general, the spectral intensity increases as the number of MCs within a sample increases. For example, the spectral intensity for $N_m = 1$ line is 4 dB higher than that of $N_m = 0$ line nearly at 7.5 MHz. Furthermore, it is about 19.6 dB greater for $N_m = 100$ curve than $N_m = 0$ line at the same ultrasonic frequency. Figure 3(c) displays that the PA amplitude increases as the number of MCs exist in a blood sample increases. The variation looks similar to that of Fig. 2(c).

Figure 4 displays envelope histograms for various samples and best fit curves for the Rayleigh, Nakagami, and generalized gamma distribution functions. These functions provide excellent fits to the histogram shown in Fig. 4(a). The generalized gamma pdf facilitates best fit to the histogram illustrated in Fig. 4(b) compared to the Rayleigh and Nakagami pdfs. The Nakagami and generalized gamma curves exhibit better agreement with the histogram data

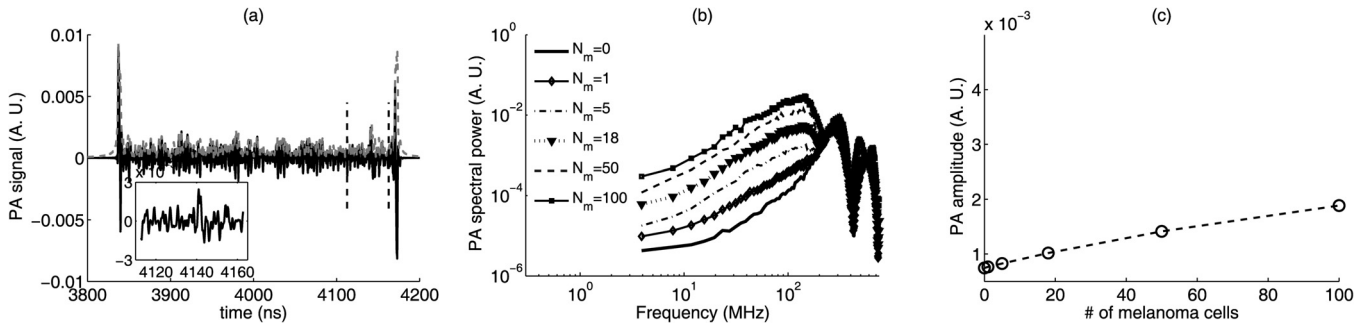

FIG. 3. A simulated PA RF line for 822 nm optical illumination when only one MC is present within the blood sample. The dashed line outlines the signal envelope. The signal from the MC and its neighboring RBCs is denoted by the two vertical lines and is further illustrated in the inset. (b) The plots of power spectrum curves (averaged over 150 RF lines for each) over a wide range of frequencies (MHz to GHz) for a series of blood samples with increasing MCs. (c) The variation of the mean PA amplitude (evaluated from 150 RF lines) as a function of MCs exist within the illuminated volume.

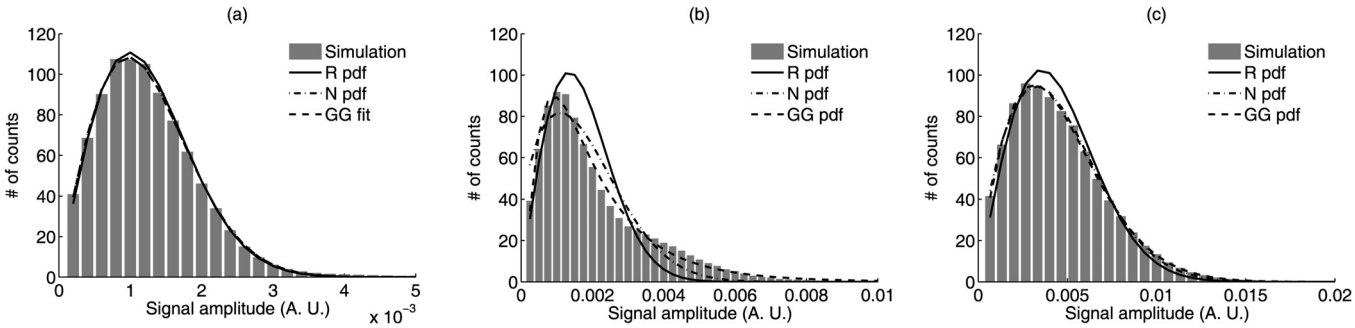

FIG. 4. (a) Average envelope histogram computed from 150 PA traces for a sample with $N_m = 1$ and $N_e = 22952$ and for 639 nm incident optical beam. The Rayleigh (R), Nakagami (N) and generalized gamma (GG) distribution curves are also shown in the same figure. (b) Same as (a) but for $N_m = 18$ and $N_e = 22850$. (c) Same as (a) but for $N_m = 100$ and $N_e = 22357$.

demonstrated in Fig. 4(c) than the Rayleigh curve. Table II presents quantitative analysis for these pdfs. Note that for clarity of the figures, bin size was arbitrarily chosen. However, bin size remained constant while the fitting parameters were estimated. The SNR for the first sample containing RBCs positioned at random locations in 3D is close to 1.91 and therefore it follows the Rayleigh statistics. The histograms appear as pre-Rayleigh as MCs in small numbers are mixed with large numbers of RBCs and associated numerical values for the SNR become less than 1.91. This deviation is maximum for the fourth sample and accordingly fitting error is maximum. The histogram is moved to a Rayleigh-like distribution as the number of MCs increases and hence fitting error is less with respect to the previous case (see rows five and six of Table II). The scale parameter (σ) of the Rayleigh distribution increases with increasing MCs in blood. The shape parameter (ξ) of the Nakagami distribution remains close to 1 for Rayleigh-like histograms and for pre-Rayleigh histograms $\xi < 1$. The variation of Ω looks similar to that of σ. It is expected, since $\Omega = 2\sigma^2$. The histograms are always better fitted with the Nakagami distribution compared to the Rayleigh distribution ($\Delta_N < \Delta_R$ for each sample). For the generalized gamma pdf, α and c parameters decrease with the introduction of MCs within the irradiating volume, reach at minimal values for the fourth sample, and after that they increase. One of the shape parameters (u) of the generalized gamma pdf initially increases with increasing MCs, becomes maximum for the fourth sample, but after that it decreases. It is also clear from Table II that fitting error for this pdf is generally less than other pdfs for each sample.

TABLE II. The estimates of the Rayleigh (R), Nakagami (N) and generalized gamma (GG) parameters for wide bandwidth signals generated at 639 nm irradiation. Fitting error [$\Delta = \sum_{i=1}^{100} (o_i - e_i)^2$, o_i, and e_i represent observed and estimated frequency, respectively] of each curve is also presented.

		R pdf		N pdf			GG pdf			
No. of cells	SNR	σ (e-4)	Δ_R	ξ	Ω (e-6)	Δ_N	α (e-4)	c	u	Δ_{GG}
$N_m = 0$ $N_e = 22958$	1.95	9.8	4.35	1.00	1.9	4.35	14.3	2.07	0.95	4.14
$N_m = 1$ $N_e = 22952$	1.77	9.9	8.71	0.96	1.9	5.94	14.2	1.98	0.97	5.93
$N_m = 5$ $N_e = 22928$	1.49	10.6	26.13	0.89	2.3	20.18	9.6	1.30	1.73	15.73
$N_m = 18$ $N_e = 22850$	1.39	13.5	59.60	0.69	4.4	39.00	0.04	0.39	10.96	16.30
$N_m = 50$ $N_e = 22657$	1.56	24.6	38.00	0.71	13.2	13.85	22.3	1.15	1.62	7.50
$N_m = 100$ $N_e = 22357$	1.75	35.6	13.83	0.86	26.2	6.23	42.2	1.53	1.29	3.56

Some representative plots of the BL signals are shown in Figs. 5(a)–5(c). Associated histograms and fitted curves are elucidated in Figs. 5(d)–5(f). Figure 5(a) presents the BL version of Fig. 2(a) and therefore, a hump appears at the same location for a MC in both the figures. Moreover, high frequency components are filtered out producing a smoother trace as shown in Fig. 5(a) relative to that of Fig. 2(a). Owing to destructive interference of tiny signals emitted by cells, signal amplitude at the central region is greatly reduced [see Fig. 5(a)] and that can also be seen in Fig. 5(d). Consequently, strong boundary buildups can be seen in this case. Figures 5(b) and 5(c) demonstrate that as the number of MCs increases, the signals originating from them occur more frequently in the RF line resulting in enhancement of signal strength in the central region. Similar observation can also be made from Figs. 5(e)–5(f). The peak of the histogram is gradually shifted from lower amplitude to higher amplitude as the concentration of MCs increases. The estimated values of various fitting parameters are presented in Table III. It can be noticed that post-Rayleigh statistics are followed by the first, fifth, and sixth samples (SNR >1.91). However, other samples obey pre-Rayleigh statistics. The Rayleigh parameter increases as the signal amplitude in the central region increases and this function provides good fits to the histograms for the fifth and sixth samples. The Nakagami shape parameter further confirms that third and fourth samples follow pre-Rayleigh statistics ($\xi < 1$). Similar to σ, Ω also increases with increasing MCs within the region of interest. As observed earlier, this distribution fits the histograms more accurately than the Rayleigh distribution. The generalized gamma parameters vary over a large range for the samples studied in this work (particularly α parameter demonstrates variation over several orders of magnitude). However, no definite trend has been observed. As expected, this pdf produces less fitting error almost in all cases confirming its flexibility to model various histograms related to diverse physical situations.

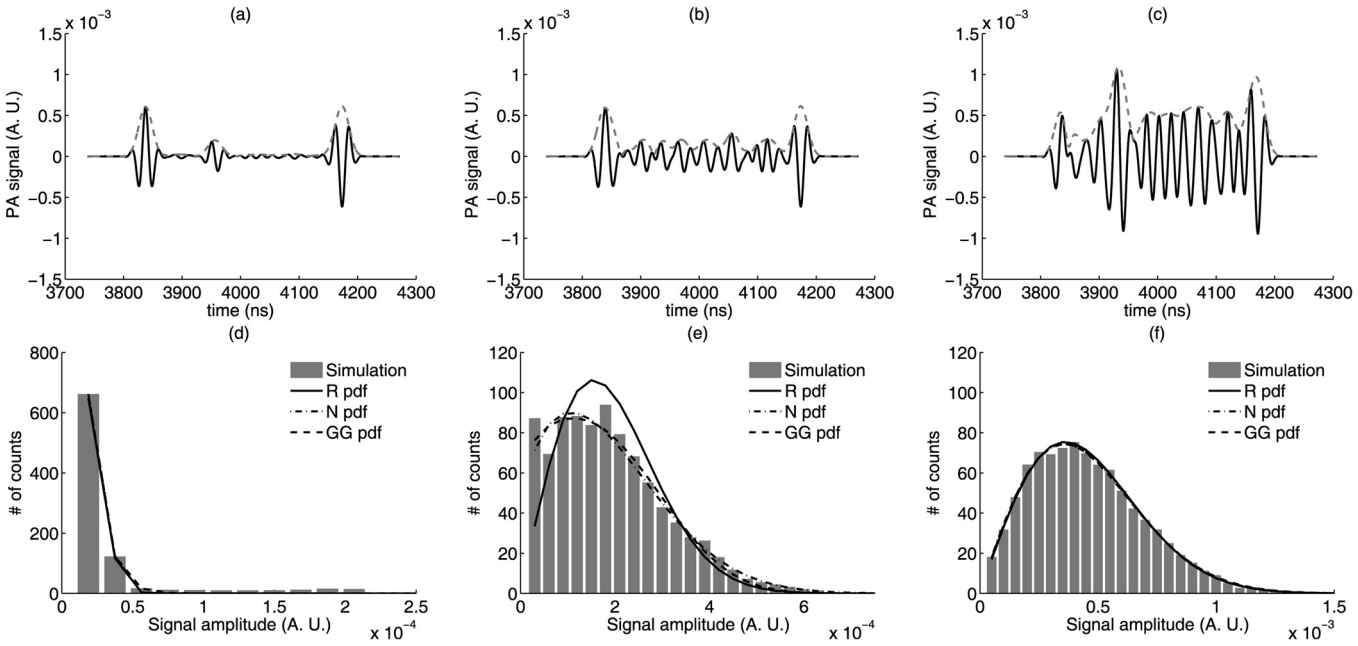

FIG. 5. (a) A typical simulated BL PA trace for a sample containing $N_m = 1$ and $N_e = 22952$ and for 639 nm illuminating radiation. The BL signal was generated for a 40 MHz transducer having 80% as the −6 dB bandwidth. (b) Same as (a) but for $N_m = 18$ and $N_e = 22850$. (c) Same as (a) but for $N_m = 100$ and $N_e = 22357$. (d) Average envelope histogram corresponding to (a) and fitted with the Rayleigh (R), Nakagami (N) and generalized gamma (GG) distribution curves. (e), (f) Same as (d) but corresponding to (b) and (c), respectively.

V. DISCUSSION AND CONCLUSIONS

A recently developed theoretical model has been employed in this study to simulate PA signals from bidisperse samples (i.e., mixtures of MCs and RBCs). The model considers each cell as a PA source and tiny signals emitted by such sources are summed up to obtain the resultant PA signal. The signal strength for a source depends upon its mechanical, thermal and optical properties. The size of the source dictates the dominant frequency content of the signal. Therefore, the model inherently incorporates the effects of physical properties and size dependence of the individual absorbers on PA signal. In other words, the model provides a framework to examine how the size, biophysical, and biochemical properties of each light absorbing object affect the PA signal.

TABLE III. The fitting parameters for the Rayleigh (R), Nakagami (N) and generalized gamma (GG) for BL signals simulated at 639 nm irradiation. The BL signals correspond to a transducer with 40 MHz center frequency and 80% as the −6 dB bandwidth. Fitting error [$\Delta = \sum_{i=1}^{100} (o_i - e_i)^2$, o_i, and e_i are the observed and estimated frequency, respectively] of each curve is also presented.

		R pdf			N pdf			GG pdf			
No. of cells	SNR	σ (e-5)	Δ_R	ξ	Ω (e-9)	Δ_N	α (e-6)	c	u	Δ_{GG}
$N_m = 0$ $N_e = 22958$	2.22	1.4	142.41	1.52	0.5	1.94	4.99	1.40	10.31	2.52
$N_m = 1$ $N_e = 22952$	1.13	1.5	50.61	1.10	0.5	38.22	6.65e-2	0.49	15.86	35.53
$N_m = 5$ $N_e = 22928$	1.13	2.3	265.60	0.35	0.5	131.23	5.17e-5	0.22	17.41	112.86
$N_m = 18$ $N_e = 22850$	1.76	15.5	53.51	0.66	52.1	24.17	322.6	2.72	0.43	21.99
$N_m = 50$ $N_e = 22657$	2.07	25.4	9.69	0.94	131.2	7.65	317.1	1.69	1.22	6.56
$N_m = 100$ $N_e = 22357$	2.13	36.2	7.75	0.98	263.2	7.54	478.6	1.83	1.12	7.35

Recently, Solano *et al.*[14] computed PA signals from hexagonally packed MCs using a time domain approach and compared simulation results with experimental findings. However, they treated each MC as a point source and the simulations were performed in 2D. The current study reports simulation results for an ensemble of spherical absorbers distributed in 3D. The 3D simulations better mimic experimental situations and may provide a means to interpret experimental data in a straightforward manner.

Another interesting result of this study is that the first minimum of power spectrum curves occurs at lower frequency for samples with MCs than that of samples with RBCs only [see Figs. 2(b) and 3(b)]. This is expected because the frequency spectrum carries size information of the absorbers. In this case, the ROI is composed of two populations of PA sources and the first two minima are linked to those sizes. Note that the oscillatory pattern exhibited by the power spectrum is due to the spherical Bessel function. For such a function, the first three minima appear when its argument becomes 4.49, 7.72, and 10.90, respectively[48] and the frequency corresponding to the first minimum can be estimated as $f = 4.49 * v_s/(2\pi a)$. Thus minima locations for MC and RBC could easily be estimated and it has been found that calculated and observed positions are in good agreement. It is known both theoretically and experimentally in the context of ultrasound backscattering that the ultrasound backscatter coefficient passes through several minima for intermixed scattering structures with different characteristic dimensions. For instance, such a variation of

backscatter coefficient was demonstrated by Roberjot *et al.*[49] experimentally for two distinct intermixed scatterer-size populations and consequently, they proved the validity of the theoretical prediction.

Absorption coefficient for MCs in this study was assumed to be the same of that of melanin. Although similar assumption was made previously by Solano *et al.*,[14] this seems to be an overestimation of the absorption coefficient for a MC. The melanin within a MC forms clusters occupying a small volume fraction of the cell. Therefore, it is expected that the actual absorption coefficient for a MC would be less than what was considered here. As a result of that signal strength for MCs would decrease with respect to the background signal arising from randomly located RBCs (i.e., contrast would be less). It would be interesting in future to appropriately estimate the absorption coefficient for MCs and then compare simulation and experimental results. Another interesting work would be to estimate the midband fit and spectral slope of various curves at different frequency bandwidths. It might be mentioned here that these parameters were found to be useful in characterizing tissue with PAs. For example, Kumon *et al.* quantified that mean PA midband fit corresponding to signals from cancerous tumor was about 9 dB higher than that of surrounding normal tissue.[22] Yang *et al.* reported that spectral slope for an artificial tumor was significantly greater than that of surrounding tissue (tumor phantom was made of agar with embedded polymer beads with 49 μm as the diameter).[23] In contrast, the mean slope greatly decreased for another artificial tumor containing 199 μm beads. Both the studies concluded that PA spectral analysis might be valuable for distinguishing tumor from normal tissue.

Simulated wide bandwidth RF lines were sampled at a very high frequency in order to illustrate sharp changes of the RF lines due to MCs [see Figs. 2(a), 3(a), and 5(a)–5(c)]. Associated SNR was computed to be around 5. It appears that MCs can be detected when high frequency signals at low amplitudes are captured at a very high sampling rate. This procedure poses a major challenge to the detection of MCs in practice. Experimental investigations also seemed to encounter similar problems. Galazha *et al.* labeled MCs with gold nanoparticles to increase SNR and thereafter detected PA signals using low frequency transducers (e.g., center frequencies at 3.5 and 20 MHz).[13] Solano *et al.* measured PA signals employing a 500 MHz transducer.[14] This paper, in the framework of forward problem formulation, demonstrates that PA spectral intensity increases significantly even in the low frequency range ($<$10 MHz) as the number of MCs increases. Consequently, it may be speculated that a frequency domain method analyzing low bandwidth signals may offer an alternative method to provide quantitative information on the average size and strength of the absorbers characterizing mixtures of MCs and RBCs. Nevertheless, further investigations are required to examine applicability of such an approach. The spectral domain analysis of PA signals may also seem to be helpful to distinguish MCs from RBC aggregates. It has been experimentally revealed that they facilitate similar contribution to the characteristics of PA signals providing additional complexity for identifying MCs in circulation.[33]

This paper also includes the statistics of the PA signals from samples composed of MCs and RBCs. The envelope histogram corresponding to PA signals generated by a large number of RBCs distributed randomly in 3D was found to follow the Rayleigh statistics. However, the envelope histograms were shifted to pre-Rayleigh regime once MCs (strong absorbers for the irradiating beam) in small numbers were mixed with large numbers of RBCs (weak absorbers at the chosen illumination). The introduction of occasional MCs resulted in a wider variation in amplitudes leading to larger standard deviation and hence, the SNR decreased. It might be mentioned here that in the context of ultrasonic tissue characterization the envelope histogram also appeared as pre-Rayleigh when strong but sparse scatterers were present in tissue.[50] Additionally, the SNRs for BL signals were computed to be more than the corresponding wide bandwidth signals and such a change could be attributed to the effect of filtering of signals. The standard deviation of a BL signal decreased due to its flat appearance causing the SNR to increase. This is consistent with the ultrasonic literature as well. For example, Tuthill[50] revealed that SNR for signal from dense scatterers shifted to a high value when low-pass filtering was performed. Additionally, it has been noticed that the generalized gamma pdf provided best fits to the histograms presented in Figs. 4 and 5. As discussed in Ref. 44, it is not surprising because it is a three-parameter function and that makes it more flexible to fit the histograms. In general, it has the ability to better fit the upper and lower tails of the histograms independently with two-shape parameters than the Rayleigh and Nakagami distributions.[44]

In conclusion, a theoretical framework to simulate PA signals from mixtures of MCs and RBCs is reported. A Monte Carlo algorithm was employed to generate random locations of impenetrable MCs and RBCs in 3D. The volume fraction occupied by the cells was about 0.4. These cells were treated as fluid spheres and were suspended in saline water. The PA signal from each cell was obtained using a frequency domain approach. Such signals were added to compute the resultant PA signal. The SNR for a MC was about 5.32 at 639 nm illumination. It allowed us to detect a MC in the RF line. Similarly, for 822 nm incident radiation the SNR was computed to be 5.40. It was found that the PA amplitude increased linearly as the number of MCs increased within the irradiated volume for those input beams. This is in qualitative agreement with experimental findings. The spectral intensity increased up to 150 MHz as the number of MCs increased. It was observed for the both incident optical radiations. For example, it was about 5.5 and 4.0 dB more at 7.5 MHz for a diseased blood sample consisting of 1 MC and 22952 RBCs in comparison to a normal blood sample with 22958 RBCs at those laser beams, respectively. This work demonstrates that histogram of envelope data generated from a sample with randomly positioned RBCs in 3D follows the Rayleigh distribution. However, histogram is shifted to pre-Rayleigh regime once MCs in small number are mixed with a large number of RBCs. Moreover, the generalized gamma distribution provides more accurate fits to the envelope histograms, generated from the samples

investigated in this work, than the Rayleigh and Nakagami distributions. The model offers a theoretical framework to study how the presence of MCs in blood alters the PA signal features. Sufficient insights regarding spectral and statistical characteristics of the PA signals from polydisperse systems can be gained from this study. Moreover, simulations results suggest that PA tissue characterization technique may be explored to analyze PA signals from MCs embedded in blood to quantify various physical parameters.

ACKNOWLEDGMENTS

This work was in part supported by CSIR, New Delhi.

[1]M. Yu, S. Stott, M. Toner, S. Maheswaran, and D. A. Harber, "Circulating tumor cells: Approaches to isolation and characterization," J. Cell Biol. **192**(3), 373–382 (2011).
[2]R. E. Payne, F. Wang, N. Su, J. Krell, A. Zebrowski, E. Yagüe, X-J. Ma, Y. Luo, and R. C. Coombes, "Viable circulating tumour cell detection using multiplex RNA *in situ* hybridisation predicts progression-free survival in metastatic breast cancer patients," Br. J. Cancer **106**, 1790–1797 (2012).
[3]R. M. Weight, J. A. Viator, P. S. Dale, C. W. Caldwell, and A. E. Lisle, "Photoacoustic detection of metastatic melanoma cells in the human circulatory system," Opt. Lett. **31**(20), 2998–3000 (2006).
[4]R. T. Krivacic, A. Ladanyi, D. N. Curry, H. B. Hsieh, P. Kuhn, D. E. Bergsrud, J. F. Kepros, T. Barbera, M. Y. Ho, L. B. Chen, R. A. Lerner, and R. H. Bruce, "A rare-cell detector for cancer," Proc. Natl. Acad. Sci. U.S.A. **101**(29), 10501–10504 (2004).
[5]L. V. Wang and S. Hu, "Photoacoustic tomography: In vivo imaging from organelles to organs," Science **335**, 1458–1462 (2012).
[6]H. F. Zhang, K. Maslov, G. Stoica, and L. V. Wang, "Functional photoacoustic microscopy for high-resolution and noninvasive *in vivo* imaging," Nat. Biotechnol. **24**, 848–851 (2006).
[7]L. V. Wang, "Prospect of photoacoustic tomography," Med. Phys. **35**(12), 5758–5767 (2008).
[8]P. Beard, "Biomedical photoacoustic imaging," Interface Focus **1**, 602–631 (2011).
[9]M. Xu and L. V. Wang, "Photoacoustic imaging in biomedicine," Rev. Sci. Instrum. **77**, 1–22 (2006).
[10]S. L. Jacques and D. J. McAuliffe, "The melanosome: threshold temperature for explosive vaporization and internal absorption coefficient during pulsed laser irradiation," Photochem. Photobiol. **53**(6), 769–775 (1991).
[11]Tabulated data from various sources complied by S. Prahl at http://omlc.ogi.edu/spectra (Last viewed February 2013).
[12]S. H. Holan and J. A. Viator, "Automated wavelet denoising of photoacoustic signals for circulating melanoma cell detection and burn image reconstruction," Phys. Med. Biol. **53**, N227–N236 (2008).
[13]E. Galanzha, E. V. Shashkov, P. M. Spring, J. Y. Suen, and V. P. Zharov, "*In vivo*, noninvasive, label-free detection and eradication of circulating metastatic melanoma cells using two-color photoacoustic flow cytometry with a diode laser," Cancer Res. **69**(20), 7926–7934 (2009).
[14]R. P. Solano, F. I. Ramirez-Perez, J. A. Castorena-Gonzalez, E. A. Anell, G. Gutiérrez-Juárez, and L. Polo-Parada, "An experimental and theoretical approach to the study of the photoacoustic signal produced by cancer cells," AIP Adv. **2**, 011102 (2012).
[15]R. K. Saha and M. C. Kolios, "A simulation study on photoacoustic signals from red blood cells," J. Acoust. Soc. Am. **129**(5), 2935–2943 (2011).
[16]E. Hysi, R. K. Saha, and M. C. Kolios, "On the use of photoacoustics to detect red blood cell aggregation," Biomed. Opt. Exp. **3**(9), 2326–2338 (2012).
[17]E. Hysi, R. K. Saha, and M. C. Kolios, "Photoacoustic ultrasound spectroscopy for red blood cell aggregation and oxygenation," J. Biomed. Opt. **17**(12), 125006 (2012).
[18]R. K. Saha and M. C. Kolios, "Effects of erythrocyte oxygenation on optoacoustic signals," J. Biomed. Opt. **16**(11), 115003 (2011).
[19]R. K. Saha, S. Karmakar, and M. Roy, "Computational investigation on the photoacoustics of malaria infected red blood cells," PLoS ONE **7**(12), e51774 (2012).
[20]R. K. Saha, M. Roy, and A. Datta, "Simulation study on the photoacoustics of cells with endocytosed gold nanoparticles," Curr. Sci. **106**(11), 1554–1559 (2014).
[21]S. Y. Nam, L. M. Ricles, L. J. Suggs, and S. Y. Emelianov, "Nonlinear photoacoustic signal increase from endocytosis of gold nanoparticles," Opt. Lett. **37**(22), 4708–4710 (2012).
[22]R. E. Kumon, C. X. Deng, and X. Wang, "Frequency-domain analysis of photoacoustic imaging data from prostate adenocarcinoma tumors in a murine model," Ultrasound Med. Biol. **37**(5), 834–839 (2011).
[23]Y. Yang, S. Wang, C. Tao, X. Wang, and X. Liu, "Photoacoustic tomography of tissue subwavelength microstructure with a narrowband and low frequency system," Appl. Phys. Lett. **101**, 034105 (2012).
[24]G. Xu, I. A. Dar, C. Tao, X. Liu, C. X. Deng, and X. Wang, "Photoacoustic spectrum analysis for microstructure characterization in biological tissue: A feasibility study," Appl. Phys. Lett. **101**, 221102 (2012).
[25]S. Wang, C. Tao, X. Wang, and X. Liu, "Quantitative detection of stochastic microstructure in turbid media by photoacoustic spectral matching," Appl. Phys. Lett. **102**, 114102 (2013).
[26]F. L. Lizzi, M. Ostromoqilsky, E. J. Feleppa, M. C. Rorke, and M. M. Yaremko, "Relationship of ultrasonic spectral parameters to features of tissue microstructure," IEEE Trans. Ultrason., Ferroelectr. Frequency Control **34**(3), 319–329 (1987).
[27]M. F. Insana, R. F. Wagner, D. G. Brown, and T. J. Hall, "Describing small-scale structure in random media using pulse-echo ultrasound," J. Acoust. Soc. Am. **87**(1), 179–192 (1990).
[28]G. J. Diebold, T. Sun, and M. I. Khan, "Photoacoustic monopole radiation in one, two and three dimensions," Phys. Rev. Lett. **67**(24), 3384–3387 (1991).
[29]G. J. Diebold, "Photoacoustic monopole radiation: Waves from objects with symmetry in one, two and three dimensions," in *Photoacoustic Imaging and Spectroscopy*, edited by L. V. Wang (Taylor and Francis Group, LLC, London, 2009), Chap. 1, pp. 3–17.
[30]A. Ishimaru, *Wave Propagation and Scattering in Random Media* (Academic, New York, 1978), Chap. 4, pp. 69–92.
[31]K. K. Shung and G. A. Thieme, *Ultrasound Scattering in Biological Tissues* (CRC Press, Boca Raton, FL, 1993), pp. 1–499.
[32]E. I. Galanzha and V. P. Zharov, "Photoacoustic flow cytometry," Methods **57**(3), 280–296 (2012).
[33]D. A. Nedosekin, M. Sarimollaoglu, E. I. Galanzha, R. Sawant, V. P. Torchilin, V. V. Verkhusha, J. Ma, M. H. Frank, A. S. Biris, and V. P. Zharov, "Synergy of photoacoustic and fluorescence flow cytometry of circulating cells with negative and positive contrasts," J. Biophoton. **6**(5), 425–434 (2013).
[34]M. d'Ischia, A. Napolitano, A. Pezzella, P. Meredith, and T. Sarna, "Chemical and structural diversity in eumelanins - unexplored bio-optoelectronic materials," Angew. Chem. Int. Ed. Engl. **48**(22), 3914–3921 (2009).
[35]G. Greco, L. Panzella, L. Verotta, M. d'Ischia, and A. Napolitano, "Uncovering the structure of human red air pheomelanin: Benzothiazolylthiazinodihydroisoquinolines as key building blocks," J. Nat. Prod. **74**, 675–682 (2011).
[36]H. Fedorow, F. Tribl, G. Halliday, M. Gerlach, P. Riederer, and K. L. Double, "Neuromelanin in human dopamine neurons: Comparison with peripheral melanins and relevance to Parkinson's disease," Progr. Neurobiol. **75**, 109–124 (2005).
[37]E. L. Hinrichsen, J. Feder, and T. Jøssang "Random packing of disks in two dimensions," Phys. Rev. A **41**(8), 4199–4209 (1990).
[38]T. Aste, "Circle, sphere, and drop packing," Phys. Rev. E **53**(3), 2571–2579 (1996).
[39]R. K. Saha and M. C. Kolios, "Effects of cell spatial organization and size distribution on ultrasound backscattering," IEEE Trans. Ultrason., Ferroelectr. Frequency Control **58**(10), 2118–2131 (2011).
[40]K. K. Shung, Y. W. Yuan, D. Y. Fei, and J. M. Tarbell, "Effect of flow disturbance on ultrasonic backscatter from blood," J. Acoust. Soc. Am. **75**, 1265–1272 (1984).
[41]M. Toubal, M. Asmani, E. Radziszewski, and B. Nongaillard, "Acoustic measurement of compressibility and thermal expansion coefficient of erythrocytes," Phys. Med. Biol. **44**, 1277–1287 (1999).
[42]R. K. Saha, S. Karmakar, E. Hysi, M. Roy, and M. C. Kolios, "Validity of a theoretical model to examine blood oxygenation dependent optoacoustics," J. Biomed. Opt. **17**(5), 055002 (2012).
[43]S. I. Fox, *Human Physiology*, 10th ed. (McGraw-Hill, New York, 2008), Chap. 13, pp. 388–430.

[44]B. I. Raju and M. A. Srinivasan, "Statistics of envelope of high-frequency ultrasonic backscatter from human skin in vivo," IEEE Trans. Ultrason., Ferroelectr. Frequency Control **49**(7), 871–882 (2002).
[45]F. Destrempes and G. Cloutier, "A critical review and uniformized representation of statistical distributions modeling the ultrasound echo envelope," Ultrasound Med. Biol. **36**(7), 1037–1051 (2010).
[46]P. M. Shankar, "A general statistical model for ultrasonic backscattering from tissues," IEEE Trans. Ultrason., Ferroelectr. Frequency Control **47**(3), 727–736 (2000).
[47]A. S. Tunis, G. J. Czarnota, A. Giles, M. D. Sherar, J. W. Hunt, and M. C. Kolios, "Monitoring structural changes in cells with high frequency ultrasound signal statistics," Ultrasound Med. Biol. **31**(8), 1041–1049 (2005).
[48]S. K. Sharma and D. J. Somerford, *Light Scattering by Optically Soft Particles Theory and Applications* (Springer-Praxis, Chichester, UK, 2006), p. 93.
[49]V. Roberjot, S. L. Bridal, P. Laugier, and G. Berger, "Absolute backscatter coefficient over a wide range of frequencies in a tissue-mimicking phantom containing two populations of scatterers," IEEE Trans. Trans. Ultrason., Ferroelectr. Frequency Control **43**(5), 970–978 (1996).
[50]T. A. Tuthill, R. H. Sperry, and K. J. Parker, "Deviations from Rayleigh statistics in ultrasonic speckle," Ultrason. Imag. **10**, 81–89 (1988).